

# Saltation-threshold model can explain aeolian features on low-air-density planetary bodies

Thomas Pähzt,<sup>1,2,\*</sup> Orencio Durán<sup>3</sup>

<sup>1</sup>Institute of Physical Oceanography, Ocean College, Zhejiang University,  
866 Yu Hang Tang Road, 310058 Hangzhou, China

<sup>2</sup>State Key Laboratory of Satellite Ocean Environment Dynamics,  
Second Institute of Oceanography, Zhejiang University,  
36 North Baochu Road, 310012 Hangzhou, China

<sup>3</sup>Department of Physical Sciences, Virginia Institute of Marine Sciences,  
College of William and Mary, PO Box 1386, Gloucester Point, 23062 Virginia, USA

\*To whom correspondence should be addressed; E-mail: 0012136@zju.edu.cn

**Knowledge of the minimal fluid speeds at which sediment transport can be sustained is crucial for understanding whether underwater landscapes exposed to water streams and wind-blown loose planetary surfaces can be altered. It also tells us whether surface features, such as ripples and dunes, can evolve. Here, guided by state-of-the-art numerical simulations, we propose an analytical model predicting the minimal fluid speeds required to sustain sediment transport in a Newtonian fluid. The model results are consistent with measurements and estimates of the transport threshold in water and Earth's and Mars' atmospheres. Furthermore, it predicts reasonable wind speeds to sustain aeolian sediment transport ("saltation") on the low-air-density planetary bodies Triton, Pluto, and 67P/Churyumov-Gerasimenko (comet). This offers**

**an explanation for possible aeolian surface features photographed on these bodies during space missions.**

When Voyager 2 photographed the surface of Neptune’s moon Triton in 1989, it revealed the occurrence of aeolian surface features, such as wind streaks and material from active plumes carried downwind (1). Likewise, New Horizons photographed similar surface features, which have been interpreted as possible wind streaks, when it passed Pluto in 2015 (2). Moreover, Rosetta photographed what appear to be ripples and dunes on the comet 67P/Churyumov-Gerasimenko (67P/C-G) in 2014 (3, 4). These observations are intriguing since the atmospheres on these planetary bodies have been considered too thin (surface pressure  $P \approx 1\text{Pa}$  on Triton and Pluto (2, 5)) for sediment transport by wind (“saltation”) to occur. In fact, it has been estimated that only very fine dust particles with mean diameters  $d \lesssim 10\mu\text{m}$  should be susceptible to transport at reasonable winds on Triton and Pluto (5, 6), and only if cohesive interparticle forces are small. However, these estimates are based on semi-empirical models, whose applicability to such extreme conditions is not well understood. Moreover, for very fine dust particles, cohesive forces are usually very large, which strongly increases the wind speeds required to sustain saltation (7) and thus further questions these estimates.

Here we propose an analytical model for the cessation threshold of sediment transport that is entirely based on physical principles. It can be applied to arbitrary Newtonian fluids and thus provides estimates of the minimal fluid speeds required to shape fluid-sheared surfaces as diverse as sea floors, riverscapes, and wind-blown loose planetary surfaces (Fig. 1). The model is consistent with measurements in water and Earth’s atmosphere and an observational estimate in Mars’ atmosphere. When applied to Triton and Pluto, it predicts that saltation of particles with  $d \in [100, 6000]\mu\text{m}$  can be sustained under 10m winds of just 30–90m/s, which can explain the observations of wind-blown features on the surfaces of these bodies.

The derivation of the analytical model is guided by state-of-the-art numerical simulations

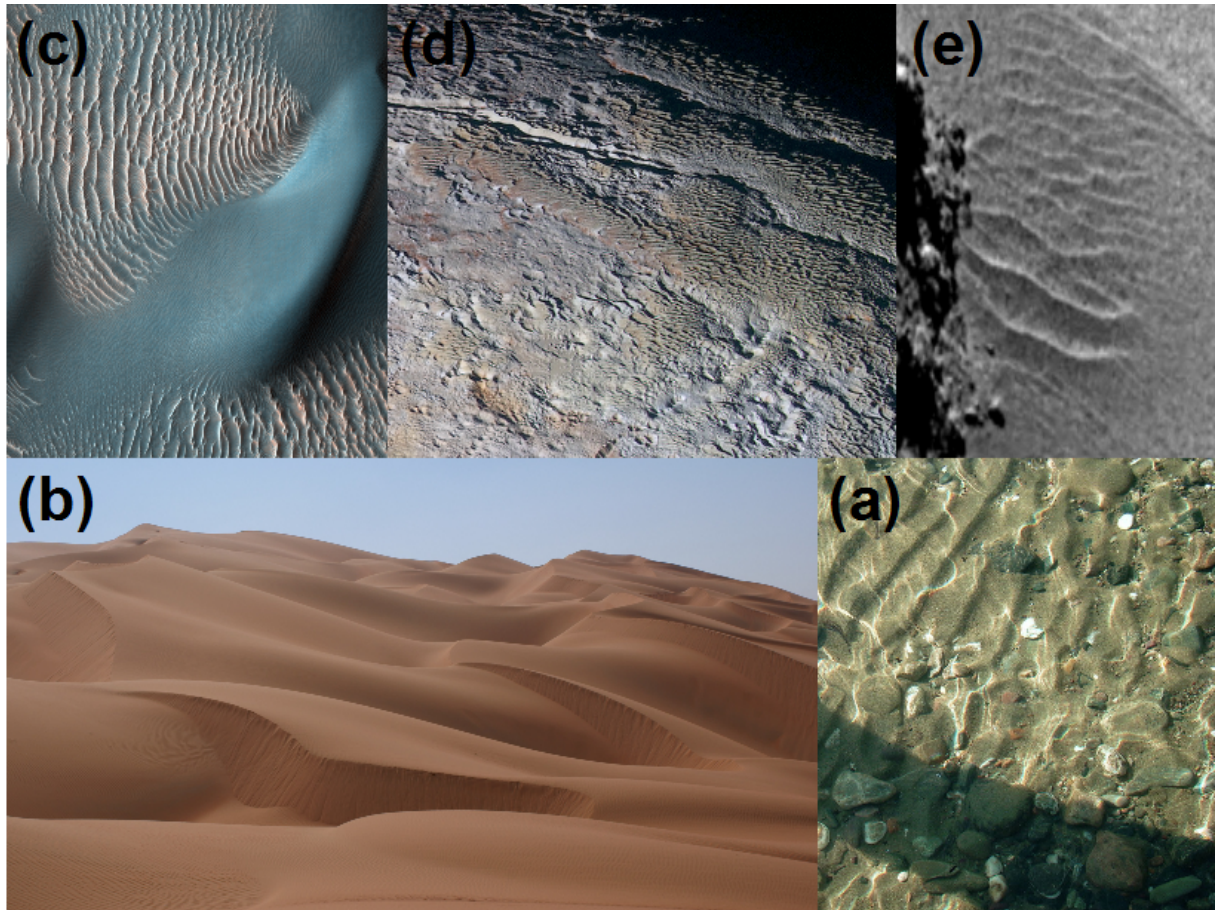


Figure 1: Surfaces shaped by fluid shear (a) under water, (b) on Earth, (c) on Mars, (d) possibly on Pluto, and (e) possibly on 67P/Churyumov-Gerasimenko. Images are from (a) [https://en.wikipedia.org/wiki/Giant\\_current\\_ripples](https://en.wikipedia.org/wiki/Giant_current_ripples) (license CC BY-SA 3.0), (b) <https://en.wikipedia.org/wiki/Desert> (license CC BY-SA 3.0), (c & d) NASA, and (e) ESA.

of steady, homogeneous sediment transport in Newtonian fluids with the numerical model of Ref. (8), which we use to test each proposed equation of the analytical model and its transport threshold predictions. This numerical model considers all particles ( $\approx 15000$ , including  $> 10$  layers of sediment bed particles) as spheres with diameters uniformly distributed between 0.8 and 1.2 times the mean diameter ( $d$ ) based on the Discrete Element Method. The fluid is modeled using the Reynolds-Averaged Navier-Stokes Equations combined with an improved mixing length approximation that can be used to calculate the turbulent mean fluid velocity at high particle concentrations. The model considers the buoyancy and fluid drag forces acting on particles, but neglects cohesive and higher-order fluid forces, such as the hindrance, added-mass, and lift force. The lubrication force, though not modeled directly, is roughly considered via varying coefficient of restitution ( $e$ ) for binary particle collisions (9). To our knowledge, this numerical model is the only one that has been shown to reproduce the different hydraulic regimes (10), the exponential decrease of the fluid velocity profile within the sediment bed (11), as well as viscous and turbulent sediment transport in water and air (8, 12), all at the same time.

We carried out simulations for particle-fluid density ratios ( $s = \rho_p/\rho_f$ ) within the range  $s \in [1.2, 2000]$  and particle Reynolds numbers ( $\text{Re} = \sqrt{(s-1)gd^3}/\nu$ ) within the range  $\text{Re} \in [0.1, 100]$ , where  $g$  is the gravity constant and  $\nu$  the kinematic viscosity. For each pair of  $s$  and  $\text{Re}$ , we varied the dimensionless fluid shear stress ( $\Theta = \tau/[(\rho_p - \rho_f)gd]$ ), which is also known as the “Shields parameter” (13), in regular intervals and obtained  $\Theta_t$  as its smallest value below which sediment transport ceases.

Fig. 2 shows the agreement between simulated values of  $\Theta_t$  and measurements in water ( $s = 2.65$ ) and Earth’s atmosphere ( $s = 2000$ ) for cohesionless sediments (13–16). It also shows simulations for typical heavy-air conditions ( $s = 100$ ), which are exemplary for the atmospheres of Venus and Titan. The slight overestimation of the experimental range of  $\Theta_t$  for subaqueous conditions by our simulations can be attributed to neglecting the hindrance

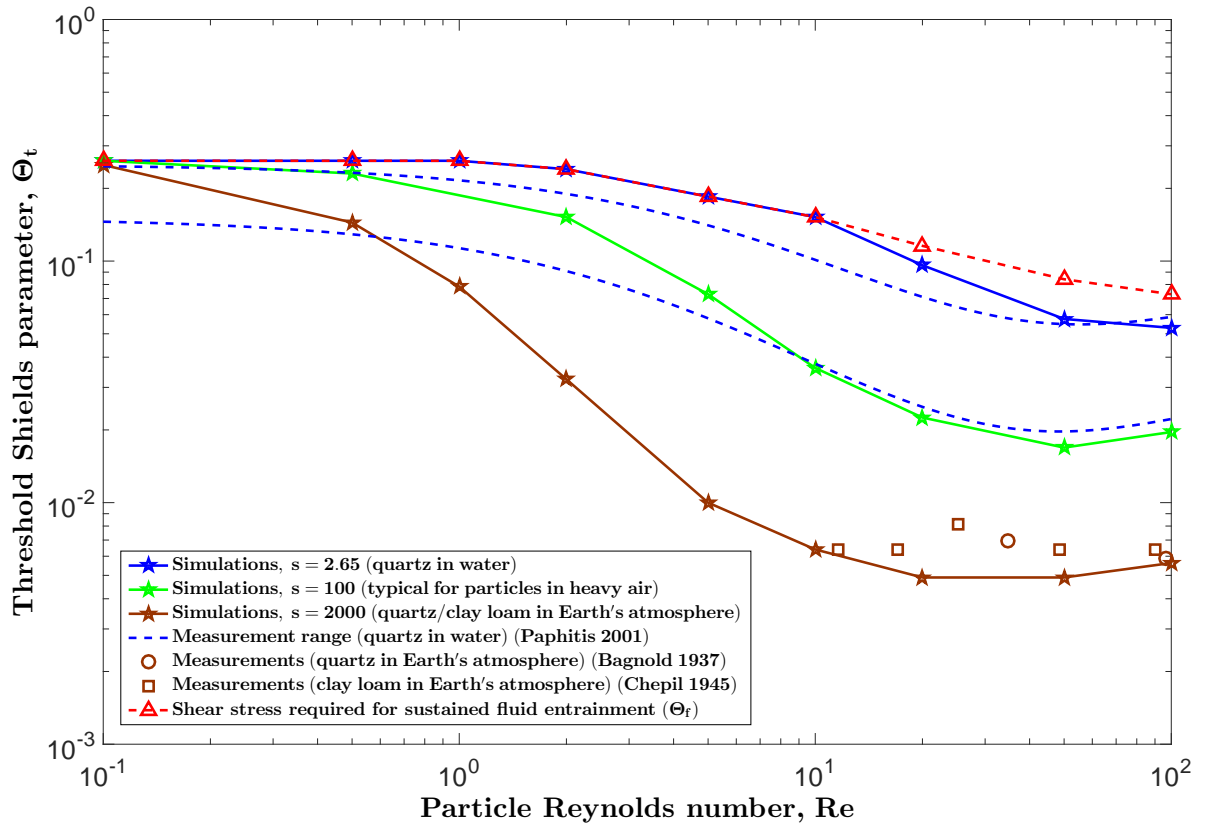


Figure 2: The threshold Shields parameter ( $\Theta_t$ ) versus the particle Reynolds number ( $Re$ ) for simulations and measurements in water (13, 14) and Earth's atmosphere (15, 16) with cohesionless sediments, and for simulations of typical heavy-air conditions.

effect (17) (supplementary online text) and to the fact that many of these subaqueous measurements were obtained through extrapolation of sediment transport rates ( $Q$ ) to (nearly) vanishing transport (13), which results in values slightly ( $\lesssim 30\%$ ) smaller than  $\Theta_t$ . In fact, in our simulations,  $Q$  does not vanish when  $\Theta - \Theta_t \rightarrow 0^+$ , which is consistent with recent theoretical and experimental studies (18–22). Fig. 2 also shows simulated values of  $\Theta_f$ , which is the  $s$ -independent value of  $\Theta$  required to sustain sediment transport solely through fluid entrainment (14). Interestingly, in most simulations,  $\Theta_f > \Theta_t$ , implying that, under threshold conditions, sediment transport is at least partially sustained through entrainment of particles of the bed top by impacts of already transported particles (see also supplementary movies). Indeed, it has been recently suggested that particle-bed impacts, which have been known to play a crucial role in sustaining sediment transport in light air, like on Earth and Mars, are also important for sustaining sediment transport in heavy air (23), like on Venus and Titan, and liquids (21), in contrast to previous believes (7, 13, 24). It is further worth noting that the lubrication force seems to have only marginal influence on the values of  $\Theta_t$  for small- $s$  conditions (for which lubrication is deemed to be relevant (9)), since we find no significant difference between simulations with  $e = 0.9$  (no lubrication) and  $e = 0.01$  (nearly maximal lubrication).

Since the system is not at rest under threshold conditions, a complete understanding of sediment transport cessation must incorporate complex particle dynamics. In the model we propose, the particle dynamics is described by the dimensionless height-averaged particle velocity ( $V = \overline{\langle v_x \rangle} / \sqrt{(s-1)gd}$ ), vertical granular temperature ( $T_z = \overline{\langle v_z^2 \rangle} / [(s-1)gd]$ ), and particle transport height ( $Z = \overline{z}/d$ ). Furthermore, the fluid dynamics at the threshold is described by  $\Theta_t$  and the dimensionless height-averaged fluid velocity ( $U = \overline{u_x} / \sqrt{(s-1)gd}$ ). The notation  $\langle \cdot \rangle$  denotes a local, mass-weighted ensemble average and the overbar a mass-density-weighted average over heights  $z > z_s$  (14). Here  $z_s$  is defined through a maximum of the particle shear work and typically located less than  $1d$  apart from the bed top (14). This definition is suggested by

our simulation results, which indicate that the friction coefficient (i.e., particle-shear-pressure ratio,  $\mu$ ) evaluated at  $z_s$  is roughly a constant with  $\Theta \geq \Theta_t$  and varies only slightly between about 0.55 and 0.85 with  $s$  and  $\text{Re}$  (Fig. S1). Since  $\mu_b = \mu(z_s)$  relates average horizontal to average vertical forces acting on particles (supplementary online text), the finding  $\mu_b = \text{const}$  provides a mean to analytically link fluid to particle quantities. Further links result from the fact that the velocity-based quantities  $U$ ,  $V$ , and  $T_z$  must be strongly correlated with each other, and that  $T_z$  controls the thickness of particle trajectories, analogous to ideal gases.

From our simulations, we find the following model equations, which can be used to simultaneously solve for  $V$ ,  $T_z$ ,  $Z$ ,  $U$ , and  $\Theta_t$ :

$$U - V = f_1(\mu_b, \text{Re}, T_z/(U - V)^2), \quad (1)$$

$$V/U = \beta_1(1 - \exp(-\beta_2\sqrt{\Theta_t})), \quad (2)$$

$$T_z = \alpha\mu_b^{-2}V^2, \quad (3)$$

$$U = \sqrt{\Theta_t}f_2(\text{Re}\sqrt{\Theta_t}, Z), \quad (4)$$

$$Z = Z_c + (s + 0.5)T_z, \quad (5)$$

where  $\mu_b = 0.77$  (consistent with Fig. S1),  $\alpha = 0.045$ ,  $\beta_1 = 0.8$ ,  $\beta_2 = 6.5$ , and  $Z_c = 0.71$  are the model parameters. Eq. (1), where  $f_1$  is a function of  $\mu_b$ ,  $\text{Re}$ , and  $T_z/(U - V)^2$ , is a direct consequence of  $\mu_b = \text{const}$  (supplementary online text). It has been analytically derived from a standard expression for the fluid drag force acting on a particle (25) and takes into account mean viscous and turbulent drag, and enhancement of mean turbulent drag due to particle-velocity fluctuations. Eq. (2) describes that the fluid forces the particles towards its own velocity, but that the magnitude of this forcing is a function of  $\Theta_t$ , which we determined from our simulations. Eq. (3) encodes that particle-bed impacts generate granular temperature (26) and thus  $T_z \propto V^2$ . The additional prefactor  $\mu_b^{-2}$  arises from the interpretation of  $\mu_b^{-1}$  as the characterization of the amount of horizontal momentum transferred into vertical momentum during such impacts (27).

Eq. (4), where  $\sqrt{\Theta_t}f_2$  is the “law of the wall”, which is an experimentally well-known function of  $\text{Re}\sqrt{\Theta_t}$  and  $z/d$  (10) (supplementary online text), is an approximate analytical implication of the assumption that the vertical profile of the fluid velocity is undisturbed by the presence of particles under threshold conditions and thus  $[u_x/\sqrt{(s-1)gd}](z/d) = \sqrt{\Theta_t}f_2(\text{Re}\sqrt{\Theta_t}, z/d)$ . It is mainly this equation that distinguishes threshold from above-threshold conditions. Eq. (5) is an approximate analytical implication of the vertical momentum balance (supplementary online text). It is also the only model equation that introduces an explicit dependency on  $s$ . Indeed, the increase of  $Z$  with  $s$  allows to maintain the same average fluid velocity ( $U$ ) with decreasing values of  $\Theta_t$  (Eq. (4)). In other words, since particles reach larger average heights with increasing  $s$ , the same average fluid force can be achieved at smaller values of  $\Theta_t$ , which is the main reason for the observed trend of  $\Theta_t$  decreasing with  $s$  (see Fig. 3).

Eqs. (1-5) are consistent with the simulation data, though the agreement between both can be significantly improved when incorporating into Eqs. (2-4) a corrective quantity  $1 < \lambda < 2$  that takes into account the vertical variation of the horizontal drag acceleration (Figs. S2-S6). In the supplementary online text, we provide and validate a further model equation that can be used to calculate  $\lambda$  (Fig. S7). However, the resulting predictions of  $\Theta_t$  from this complexer model do not deviate much from the predictions by Eqs. (1-5) (Figs. S8-S10), indicating that the model predictions are quite robust to the precise conceptual modeling.

Fig. 3 shows  $\Theta_t$  predicted by the analytical model in various environments versus the transport-layer Reynolds number ( $\text{Re}_t = \text{Re}\sqrt{s}$ ). The analytical model is consistent with measurements in water (13) and Earth’s atmosphere (15, 16) for cohesionless sediments, even though it has not been fitted to these data (for a comparison to the numerical data, see Fig. S8). Moreover, the analytical model is consistent with an observational estimate from seasonal variations of  $Q$  on the Nili Patera dune field, Mars (14, 28) (dash-dotted lines), where the displayed bounds of  $\text{Re}_t$  correspond to cohesionless particles with  $d \in [570, 910]\mu\text{m}$ , which was inferred from

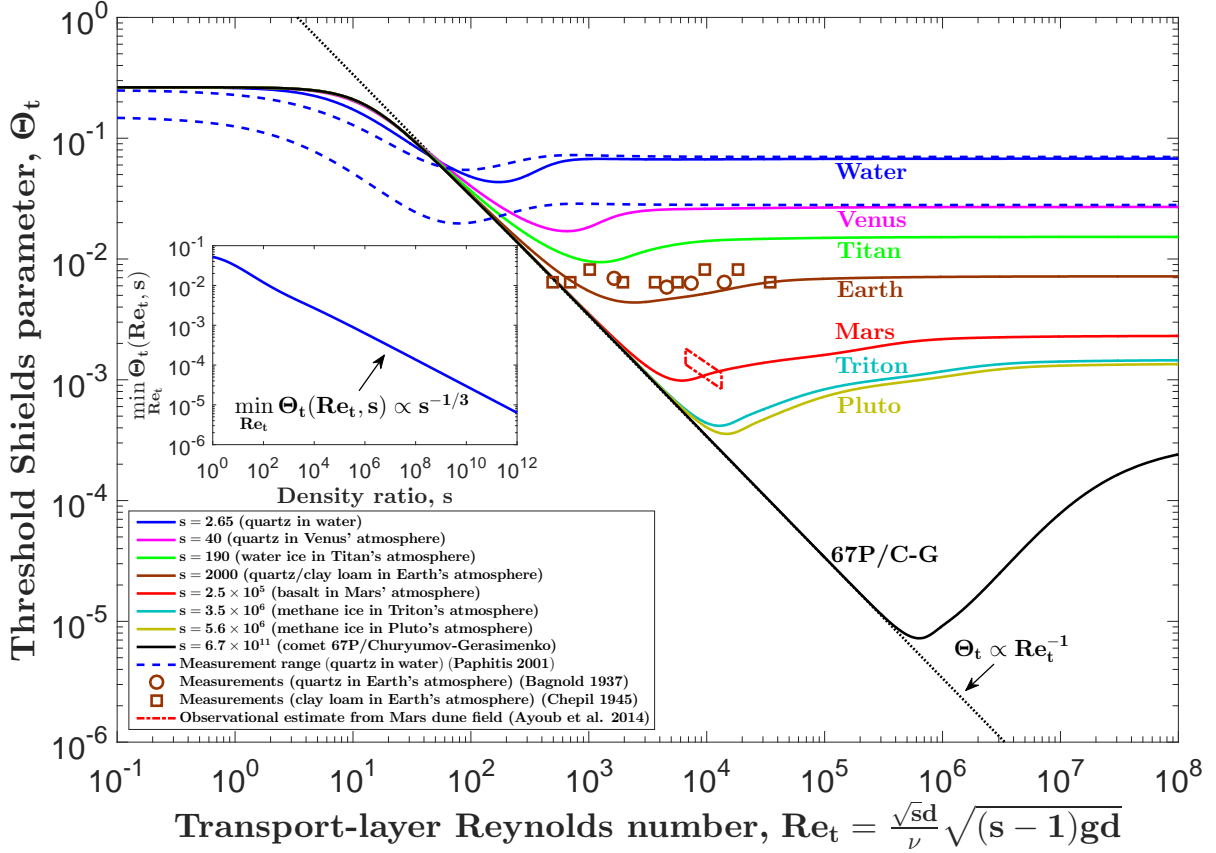


Figure 3: The threshold Shields parameter ( $\Theta_t$ ) in various environments predicted by the analytical model (solid lines), measured in water (13) (dashed lines) and Earth's atmosphere (15, 16) (symbols) for cohesionless sediments, and observationally estimated from seasonal variations of  $Q$  on Mars (14, 28) versus the transport-layer Reynolds number ( $Re_t$ ). Inset:  $\min_{Re_t} \Theta_t(Re_t, s)$  versus  $s$ .

thermal emission spectra of Mars dunes (29).

To obtain reliable predictions for cohesive sediments, it is necessary to include the influences of cohesive interparticle forces in the analytical model. Here we use the cohesion correction by Ref. (30), which corrects the resistance to surface shear and thus  $\mu_b$  through  $\mu_b^{\text{corr}}/\mu_b = 1 + 1.5(d_m/d)^{5/3}$ , where  $d_m/(25\mu\text{m}) = \{2650\text{kg/m}^3 \times 9.81\text{m/s}^2 / [(\rho_p - \rho_f)g]\}^{2/5}$ . Fig. 4 shows the threshold fluid shear velocity ( $u_t = \sqrt{\Theta_t(s-1)gd}$ ) predicted by the analytical model for the same natural environments as before versus the mean particle diameter ( $d$ ). The solid (dashed) lines thereby correspond to the predictions corrected (uncorrected) for cohesive interparticle forces. Moreover, in contrast to Figs. 2 and 3, measurements in Earth's atmosphere for cohesive sediments are now also included.

It can be seen that the analytical model predicts fairly extreme threshold wind shear velocities necessary to sustain saltation on 67P/Churyumov-Gerasimenko ( $u_t = 50 - 200\text{m/s}$  for  $d = 10 - 1\text{mm}$ ). This prediction is consistent with estimated wind shear velocities of up to  $500\text{m/s}$ , which may occur over short distances in the region where the ripples are located due to enormous pressure gradients resulting from fluid flow into the vacuum (4). Moreover, the predicted values of  $u_t$  on Triton and Pluto are between about  $1.4\text{m/s}$  and  $3.7\text{m/s}$  for particles sizes in the range  $d \in [100, 6000]\mu\text{m}$ . They correspond to  $10\text{m}$  winds ( $u_{10m}$ ) between  $30\text{m/s}$  and  $90\text{m/s}$ , which is about an order of magnitude smaller than previous predictions (6) and comparable to wind speeds during storms on Earth and Mars (7). This suggests that wind-blown surfaces on these planetary bodies can become mobile and evolve into aeolian features much more easily than previously thought, which thus supports the hypothesis that the surface features photographed on these bodies are, indeed, of aeolian origin. Moreover, the minimal value  $u_t \approx 1.4\text{m/s}$  ( $u_{10m} \approx 30\text{m/s}$ ) is predicted to occur for rather large particles of about  $1\text{mm}$  size. We thus postulate that aeolian surface features predominantly consist of coarse sand rather than fine dust on Triton and Pluto. Because wind speeds required to sustain saltation are well below

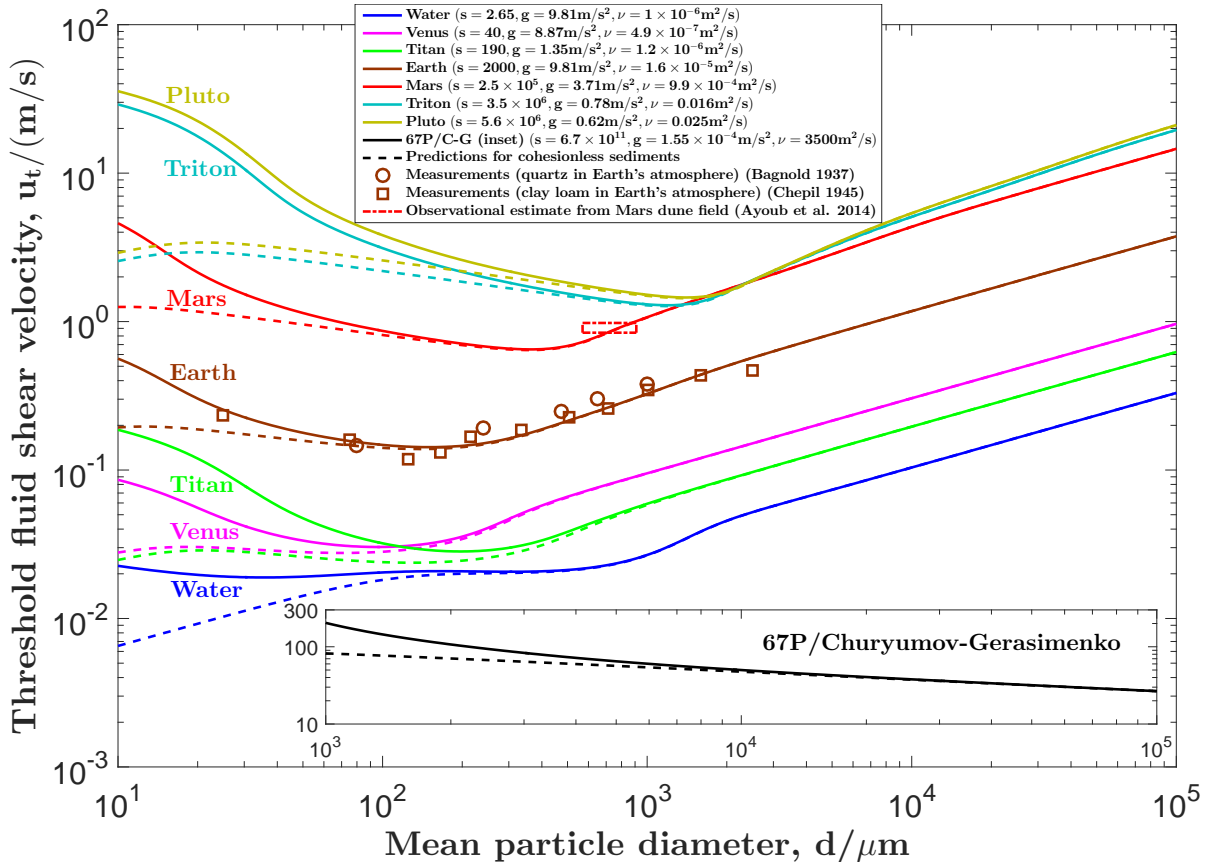


Figure 4: The threshold fluid shear velocity ( $u_t$ ) in various environments predicted by the analytical model corrected (solid lines) and uncorrected (dashed lines) for cohesive interparticle forces versus the mean particle diameter ( $d$ ). The symbols correspond to measurements in Earth's atmosphere (15, 16) and the red, dash-dotted lines to an observational estimate from seasonal variations of  $Q$  on Mars (14, 28).

those required to initiate saltation in low-air-density environments (7), an initiation mechanism distinct from wind erosion might be involved. On Triton, geyser-like eruptions provide such a mechanism (1, 5), and possibly also on Pluto (6). Another possible candidate are nitrogen-ice particles forming in midair from desublimation when air temperatures fall. In summary, our study suggests that surface-shaping transport of sediment by wind might be far more common than previously thought on planetary bodies with extremely thin atmospheres.

## References

1. C. J. Hansen, A. S. McEwen, A. P. Ingersoll, R. J. Terrile, *Science* **250**, 421 (1990).
2. S. A. Stern, *et al.*, *Science* **350**, aad1815 (2015).
3. N. Thomas, *et al.*, *Science* **347**, aaa0440 (2015).
4. N. Thomas, *et al.*, *Astronomy & Astrophysics* **583**, A17 (2015).
5. C. Sagan, C. Chyba, *Nature* **346**, 546 (1990).
6. J. M. Moore, *et al.*, *Icarus* **246**, 65 (2015).
7. J. F. Kok, E. J. R. Parteli, T. I. Michaels, D. B. Karam, *Reports on Progress in Physics* **75**, 106901 (2012).
8. O. Durán, B. Andreotti, P. Claudin, *Physics of Fluids* **24**, 103306 (2012).
9. P. Gondret, M. Lance, L. Petit, *Physics of Fluids* **14**, 2803 (2002).
10. J. Guo, P. Y. Julien, *The Fifth International Symposium on Environmental Hydraulics (ISEH V)*, Tempe, Arizona (University of Nebraska - Lincoln, 2007), vol. Paper 5, pp. 1–6.
11. A. Hong, M. Tao, A. Kudrolli, *Physics of Fluids* **27**, 013301 (2015).
12. O. Durán, B. Andreotti, P. Claudin, *Advances in Geosciences* **37**, 73 (2014).
13. D. Paphitis, *Coastal Engineering* **43**, 227 (2001).
14. See supplementary materials for the (fluctuation) energy balances and their uses in the derivation.
15. R. A. Bagnold, *The Geographical Journal* **89**, 409 (1937).

16. W. S. Chepil, *Soil Science* **60**, 397 (1945).
17. J. F. Richardson, W. N. Zaki, *Transactions of the Institution of Chemical Engineers* **32**, 35 (1954).
18. M. V. Carneiro, T. Pähzt, H. J. Herrmann, *Physical Review Letters* **107**, 098001 (2011).
19. M. V. Carneiro, K. R. Rasmussen, H. J. Herrmann, *Scientific Reports* **5**, 1 (2015).
20. M. Houssais, C. P. Ortiz, D. J. Durian, D. J. Jerolmack, *Nature Communications* **6**, 6527 (2015).
21. A. H. Clark, M. D. Shattuck, N. T. Ouellette, C. S. O’Hern, *Physical Review E* **92**, 042202 (2015).
22. R. Maurin, J. Chauchat, B. Chareyre, P. Frey, *Physics of Fluids* **27**, 113302 (2015).
23. D. Berzi, J. T. Jenkins, A. Valance, *Journal of Fluid Mechanics* **786**, 190 (2016).
24. D. M. Burr, *et al.*, *Nature* **517**, 60 (2015).
25. B. Camenen, *Journal of Hydraulic Engineering* **133**, 229 (2007).
26. T. Pähzt, O. Durán, T.-D. Ho, A. Valance, J. F. Kok, *Physics of Fluids* **27**, 013303 (2015).
27. J. T. Jenkins, A. Valance, *Journal of Fluid Mechanics* **26**, 073301 (2014).
28. F. Ayoub, *et al.*, *Nature Communication* **5**, 5096 (2014).
29. L. K. Fenton, J. L. Bandfield, A. W. Ward, *Journal of Geophysical Research* **108**, 5129 (2003).
30. P. Claudin, B. Andreotti, *Earth and Planetary Science Letters* **252**, 30 (2006).

31. We acknowledge support from grants National Natural Science Foundation of China (Nos. 1151101041 and 41376095) and Natural Science Foundation of Zhejiang Province (No. LR16E090001).

## Materials and Methods

### Planetary conditions

#### Venus

We assume that Venus' particles consist of quartz ( $\rho_p = 2650\text{kg/m}^3$ ) and Venus' air to 96.5% of CO<sub>2</sub> and 3.5% of N<sub>2</sub> with pressure  $P = 9.2 \times 10^6\text{Pa}$  and temperature  $T = 737\text{K}$ . This corresponds to  $s \approx 40$  and  $\nu \approx 4.9 \times 10^{-7}\text{m}^2/\text{s}$  (cf. (24)). The gravitational constant is taken as  $g = 8.87\text{m/s}^2$ .

#### Titan

We assume that Titan's particles consist of water ice ( $\rho_p = 1000\text{kg/m}^3$ ), and that Titan's air has a density  $\rho_f = 5.3\text{kg/m}^3$ , corresponding to  $s = 190$ , and viscosity  $\nu = 1.2 \times 10^{-6}\text{m}^2/\text{s}$  (24). The gravitational constant is taken as  $g = 1.35\text{m/s}^2$ .

#### Earth

We assume that Earth's particles consist of quartz or clay loam as in the experiments of Refs. (15, 16) ( $\rho_p = 1650 - 2650\text{kg/m}^3$ ), and that Earth's air has a density  $\rho_f = 1.2\text{kg/m}^3$ , corresponding to  $s = 1350 - 2210$ , and viscosity  $\nu = 1.6 \times 10^{-5}\text{m}^2/\text{s}$ . Since most particles in the experiments are in the upper end of the density range, we choose  $s = 2000$ . Note that the choice of  $s$  does not much affect the agreement with the experiments. The gravitational constant is taken as  $g = 9.81\text{m/s}^2$ .

## Mars

We assume that Mars' particles consist of basalt ( $\rho_p = 3000\text{kg/m}^3$ ) and Mars' air to 96% of CO<sub>2</sub> and 2% of N<sub>2</sub> and 2% of Ar with  $P = 520\text{Pa}$  and  $T = 230\text{K}$  (28). This corresponds to  $s \approx 2.5 \times 10^5$  and  $\nu \approx 9.9 \times 10^{-4}\text{m}^2/\text{s}$ . The gravitational constant is taken as  $g = 3.71\text{m/s}^2$ .

## Triton

We assume that Triton's particles consist of methane ice ( $\rho_p = 500\text{kg/m}^3$ ) and Triton's atmosphere of N<sub>2</sub> with  $P = 1.6\text{Pa}$  and  $T = 38\text{K}$  (5). This corresponds to  $s \approx 3.5 \times 10^6$  and  $\nu \approx 0.016\text{m}^2/\text{s}$ . The gravitational constant is taken as  $g = 0.78\text{m/s}^2$ .

## Pluto

We assume that Pluto's particles consist of methane ice ( $\rho_p = 500\text{kg/m}^3$ ) and Pluto's atmosphere of N<sub>2</sub> with  $P = 1\text{Pa}$  and  $T = 38\text{K}$  (2). This corresponds to  $s \approx 5.6 \times 10^6$  and  $\nu \approx 0.025\text{m}^2/\text{s}$ . The gravitational constant is taken as  $g = 0.62\text{m/s}^2$ .

## 67P/Churyumov-Gerasimenko

From numerical simulations, it has been estimated that the air-molecule-number density is about  $5 \times 10^{16}\text{m}^{-3}$  (4). Assuming  $\rho_p \approx 1000\text{kg/m}^3$  (organics) and that the air consists predominantly of H<sub>2</sub>O with  $T = 200\text{K}$  (4), this corresponds to  $s \approx 6.7 \times 10^{11}$  and  $\nu \approx 5300\text{m}^2/\text{s}$ . The gravitational constant is taken as  $g = 1.55 \times 10^{-4}\text{m/s}^2$  (4).

## Local average transport quantities and balance laws

The manner in which we obtain the local average transport quantities from our numerical simulations is described in detail in Ref. (26) and its supplementary material. Here we summarize those of their results that are essential for understanding the math and physics behind the symbols and equations in the paper.

We presume that we have performed numerical simulations and collected data for  $N$  subsequent constant time steps  $\delta t$ . The ensemble average, denoted by  $\bar{\cdot}^E$ , of a quantity  $A$  can then be estimated as the time average,

$$\bar{A}^E \approx \frac{1}{N} \sum_{i=1}^N A_i, \quad (\text{S1})$$

where  $A_i$  is the quantity  $A$  evaluated for the  $i$ -th time step. The ensemble average is used to define the mass density ( $\rho$ ) and the local, mass-weighted ensemble average, denoted by  $\langle \cdot \rangle$ , of a quantity  $A$  as

$$\rho = \overline{\sum_n m^n \delta(\mathbf{x} - \mathbf{x}^n)}^E, \quad (\text{S2})$$

$$\langle A \rangle = \frac{1}{\rho} \overline{\sum_n m^n A^n \delta(\mathbf{x} - \mathbf{x}^n)}^E, \quad (\text{S3})$$

where the superscript 'n' of a quantity refers to its value for the particle with the number  $n$ . In the simulations, these sums of delta distributions are coarse-grained through averaging over the discretized space elements (26).

In the supplementary material of Ref. (26), local mass, momentum, and (fluctuation) energy balance laws in many different forms are derived solely from Newton's axioms. Those ones that are essential to understanding the paper read (Einsteinian summation)

$$\langle v_z \rangle = 0, \quad (\text{S4})$$

$$\frac{dP_{zi}}{dz} = \rho \langle a_i \rangle, \quad (\text{S5})$$

where  $\mathbf{a}$  is the acceleration due to external forces (i.e., gravity and fluid forces) and  $\mathbf{a}^c$  the acceleration due to contact forces. Furthermore,  $P_{ij}$  is the particle stress tensor, which is separated into a transport (superscript 't') and a contact contribution (superscript 'c'), reading

$$P_{ij} = P_{ij}^t + P_{ij}^c, \quad (\text{S6})$$

$$P_{ij}^t = \rho \langle c_i c_j \rangle, \quad (S7)$$

$$P_{ij}^c = \frac{1}{2} \overline{\sum_{mn} F_j^{mn} (x_i^m - x_i^n) \int_0^1 \delta(\mathbf{x} - (\mathbf{x}^m - \mathbf{x}^n)s + \mathbf{x}^n) ds}, \quad (S8)$$

where  $\mathbf{F}^{mn} = -\mathbf{F}^{nm}$  is the contact force applied by particle  $n$  on particle  $m$  ( $\mathbf{F}^{mm} = 0$ ) and  $\mathbf{c} = \mathbf{v} - \langle \mathbf{v} \rangle$  the fluctuation velocity.

## Two heights characterizing the top of the sediment bed

In our simulations, which take into account  $> 10$  layers of particles of the sediment bed, determining the top of the sediment bed ( $z_b$ ) is not trivial. We use the definition by Ref. (8), which results in vertical locations close to the top obtained from visual inspection (20). Namely,  $z_b$  is defined as the height at which the local concentration of particles equals 50% of the concentration deep within the bed ( $\rho(z_b) = 0.5\rho_b \approx 0.29\rho_p$ ).

The height  $z_s$ , where we evaluate the friction coefficient ( $\mu$ ), is defined through a maximum of the particle shear work, reading

$$\max \left[ -P_{zx} \frac{d\langle v_x \rangle}{dz} \right] = \left[ -P_{zx} \frac{d\langle v_x \rangle}{dz} \right] (z_s). \quad (S9)$$

This definition results in heights that are usually less than  $1d$  apart from  $z_b$ . Note that, while  $\mu_b = \mu(z_s)$  is generally roughly constant with  $\Theta$ ,  $\mu(z_b)$  is not (not shown).

## Height-averaged transport quantities

We define two different height averages of a quantity  $A$ : the particle-flux-weighted average over heights  $z > z_s$ ,

$$\overline{A}^q = \frac{\int_{z_s}^{\infty} \rho \langle v_x \rangle A dz}{\int_{z_s}^{\infty} \rho \langle v_x \rangle dz} \quad (S10)$$

and the  $\rho$ -weighted average over heights  $z > z_s$ ,

$$\overline{A} = \frac{\int_{z_s}^{\infty} \rho A dz}{\int_{z_s}^{\infty} \rho dz}, \quad (\text{S11})$$

which is the one appearing in the paper.

## Measurements of $\Theta_t$

The measurements of  $\Theta_t$  in Earth's atmosphere of Refs. (15) and (16) were obtained as the smallest values of  $\Theta$  below which sediment transport ceases and are therefore directly comparable to the simulated values of  $\Theta_t$  in Fig. 2 of the paper. However, many of the subaqueous measurements displayed in the Shields diagram by Ref. (13) and the observational estimate of Ref. (28) were obtained through extrapolation of  $Q$  to (nearly) vanishing sediment transport, which results in slightly smaller values than  $\Theta_t$ . Note that comparisons of the numerical and analytical models to recent measurements of the saltation initiation threshold in heavy air of Ref. (24) were not included because it is unclear how exactly the initiation threshold relates to the cessation threshold in the light of our finding that saltation in heavy air is dominantly sustained through particle-bed-impact entrainment.

## Measurements for cohesionless sediments

The measurements of  $\Theta_t$  in Earth's atmosphere of Refs. (15) and (16) with  $d < 125\mu\text{m}$  are significantly influenced by cohesive interparticle forces and thus excluded in Figs. 2 and 3 of the paper, but included in Fig. 4. All experiments corresponding to the measurements displayed in the Shields diagram by Ref. (13) were carried out using cohesionless sediments.

## Obtaining $\Theta_f$ from the simulations

The Shields parameter required to sustain particle entrainment directly by the fluid alone ( $\Theta_f$ ) is found through looking for the maximum value of  $\sqrt{\Theta}$  (by increasing  $\sqrt{\Theta}$  with increment  $\delta\sqrt{\Theta} = 0.01$ ) at which the trivial steady solution (sediment bed at rest) is still a solution of the numerical model equations.  $\sqrt{\Theta_f}$  is then defined as the  $\delta\sqrt{\Theta}$ -incremented value of this maximum.

## Supplementary Online Text

### Influence of particle hindrance

The hindrance effect, which is neglected in our numerical and analytical models, increases the drag force acting on particles in the presence of neighboring particles by about factor  $(1-\phi)^{-3.1}$ , where  $\phi = \rho/\rho_p$  is the particle volume fraction (17). If the transport layer is sufficiently large,  $\phi$  will typically be very small at typical transport heights, and this effect can thus be neglected. However, for sediment transport as bedload (i.e, transport layer thickness of the order of  $d$ ), the hindrance effect might be significant since typical values of  $\phi$  can be as large as 0.3 (particularly in our viscous bedload simulations), corresponding to a decrease of  $\Theta_t$  by up to factor 3 for viscous and factor 1.7 for turbulent bedload. This is the reason why we believe that the slight overestimation of the subaqueous measurements of  $\Theta_t$  by our numerical and analytical models is mainly due to neglecting the hindrance effect.

## Further clarification and validation of the analytical model

### The friction coefficient ( $\mu_b$ )

Using Eqs. (S5) and (S11), the friction coefficient ( $\mu_b$ ) obeys

$$\mu_b = -\frac{P_{zx}}{P_{zz}}(z_s) = \frac{\int_{z_s}^{\infty} \frac{dP_{zx}}{dz} dz}{\int_{z_s}^{\infty} \frac{dP_{zz}}{dz} dz} = -\frac{\int_{z_s}^{\infty} \rho \langle a_x \rangle dz}{\int_{z_s}^{\infty} \rho \langle a_z \rangle dz} = -\frac{\overline{\langle a_x \rangle}}{\overline{\langle a_z \rangle}}. \quad (\text{S12})$$

Furthermore, using that the added-mass correction  $(1 - c_m/s)$ , where  $c_m = 0.5$  ( $c_m = 0$  in our simulations, which neglect the added-mass force), appears in both  $a_x$  and  $a_z$  and is thus canceled out, and approximating that the remaining vertical forces are dominated by gravity and buoyancy, it follows

$$\mu_b \approx \overline{\langle a_x^d \rangle} / \tilde{g}, \quad (\text{S13})$$

where  $\tilde{g} = (s - 1)g/s$  is the buoyancy-reduced gravity constant. Fig. S1 shows that  $\mu_b$  is roughly constant with  $\Theta \geq \Theta_t(s, \text{Re})$  for fixed  $s$  and  $\text{Re}$ . However, the value of  $\mu_b$  slightly varies between 0.55 and 0.85 depending on  $s$  and  $\text{Re}$ .

### Deriving an expression for $U - V$

The drag force acting on a particle with diameter  $d$  is given by (25)

$$\mathbf{F}^d = \frac{\rho_f \pi d^2}{8} \left[ \left( \frac{24\sqrt{(s-1)gd}}{\text{Re}} \right)^{1/m} + (C_d^\infty |\mathbf{v}_r|)^{1/m} \right]^m \mathbf{v}_r, \quad (\text{S14})$$

where  $C_d^\infty = 1$  and  $m = 1.5$  for naturally-shaped particles ( $C_d^\infty = 0.5$  and  $m = 2$  in our simulations) and  $\mathbf{v}_r = \mathbf{u} - \mathbf{v}$  is the difference between fluid and particle velocity. Using Eq. (S14) and  $a_x^d = 6F_x^d/(\rho_p \pi d^3)$ , Eq. (S13) leads to

$$\frac{4}{3} \mu_b \approx \overline{\left[ \left( \frac{24\tilde{v}_{rx}}{\text{Re}} \right)^{1/m} + (C_d^\infty |\tilde{\mathbf{v}}_r| \tilde{v}_{rx})^{1/m} \right]^m}$$

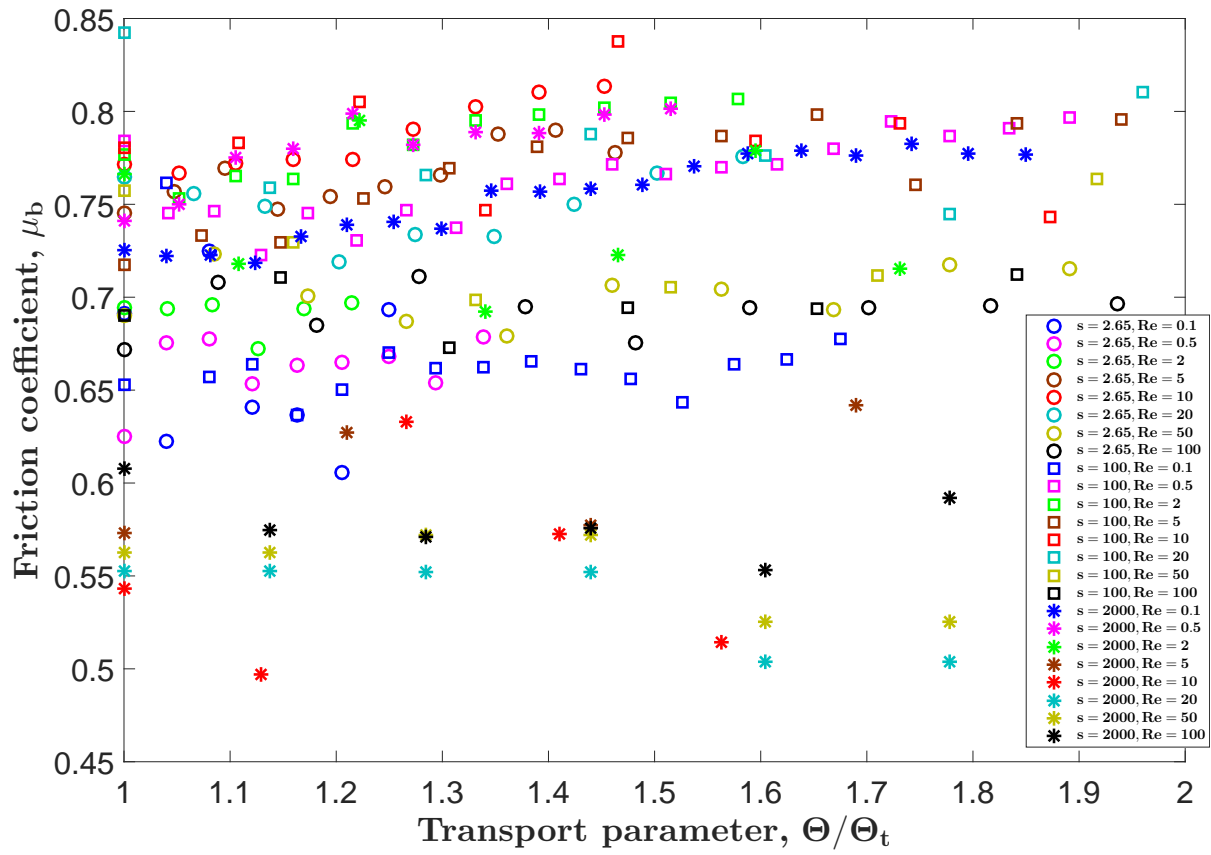


Figure S1: Simulated values of the friction coefficient ( $\mu_b$ ) versus the transport parameter ( $\Theta/\Theta_t$ ) for varying  $s$  and  $Re$ .

$$\approx \left[ \left( \frac{24 \langle \tilde{v}_{rx} \rangle}{\text{Re}} \right)^{1/m} + (C_d^\infty \overline{\langle |\tilde{\mathbf{v}}_r| \tilde{v}_{rx} \rangle})^{1/m} \right]^m, \quad (\text{S15})$$

where we neglected correlations, and the tilde henceforth denotes that velocity-based quantities are made dimensionless by the velocity scale  $\sqrt{(s-1)gd}$ . Now, neglecting fluctuations of the fluid velocity and third-order correlation of the particle velocity, we approximate

$$\langle |\tilde{\mathbf{v}}_r| \tilde{v}_{rx} \rangle \approx \langle \tilde{v}_{rx} \rangle \langle |\tilde{\mathbf{v}}_r| \rangle + \langle \tilde{c}_x^2 \rangle, \quad (\text{S16})$$

where  $\tilde{c} = \tilde{v} - \langle \tilde{v} \rangle$  is the dimensionless particle fluctuation velocity. From our simulations, we find that particle velocity fluctuations are usually negligible when compared to  $\langle v_{rx} \rangle$ . Only for bedload conditions do they become significant, for which these fluctuations are nearly isotropic ( $\langle c_x^2 \rangle \approx \langle v_y^2 \rangle \approx \langle v_z^2 \rangle$ ;  $v_y = 0$  and  $\langle c_x^2 \rangle \approx \langle v_z^2 \rangle$  in our two-dimensional simulations). We thus further approximate

$$\overline{\langle |\tilde{\mathbf{v}}_r| \tilde{v}_{rx} \rangle} \approx (U - V) \sqrt{(U - V^2) + (\text{dim} - 1)T_z} + T_z, \quad (\text{S17})$$

where  $\text{dim}$  is the number of dimensions. Inserting Eq. (S17) in Eq. (S15), we thus obtain

$$\frac{4}{3} \mu_b \approx \left[ \left( \frac{24}{\text{Re}} \right)^{1/m} + (C_d^{\text{eff}}(U - V))^{1/m} \right]^m (U - V), \quad (\text{S18})$$

where

$$C_d^{\text{eff}} = C_d^\infty \left[ \sqrt{1 + \frac{(\text{dim} - 1)T_z}{(U - V)^2}} + \frac{T_z}{(U - V)^2} \right]. \quad (\text{S19})$$

Finally, rearranging for  $U - V$  yields

$$\begin{aligned} U - V &\approx f_1 \left( \mu_b, \text{Re}, \frac{T_z}{(U - V)^2} \right), \\ f_1 \left( \mu_b, \text{Re}, \frac{T_z}{(U - V)^2} \right) &= \left[ \sqrt{\frac{1}{4} \left( \frac{24}{\text{Re}C_d^{\text{eff}}} \right)^{2/m} + \left( \frac{4\mu_b}{3C_d^{\text{eff}}} \right)^{1/m}} - \frac{1}{2} \left( \frac{24}{\text{Re}C_d^{\text{eff}}} \right)^{1/m} \right]^m, \end{aligned} \quad (\text{S20})$$

which is Eq. (1) of the paper. Fig. S2 shows that Eq. (S20) is consistent with the simulation data.

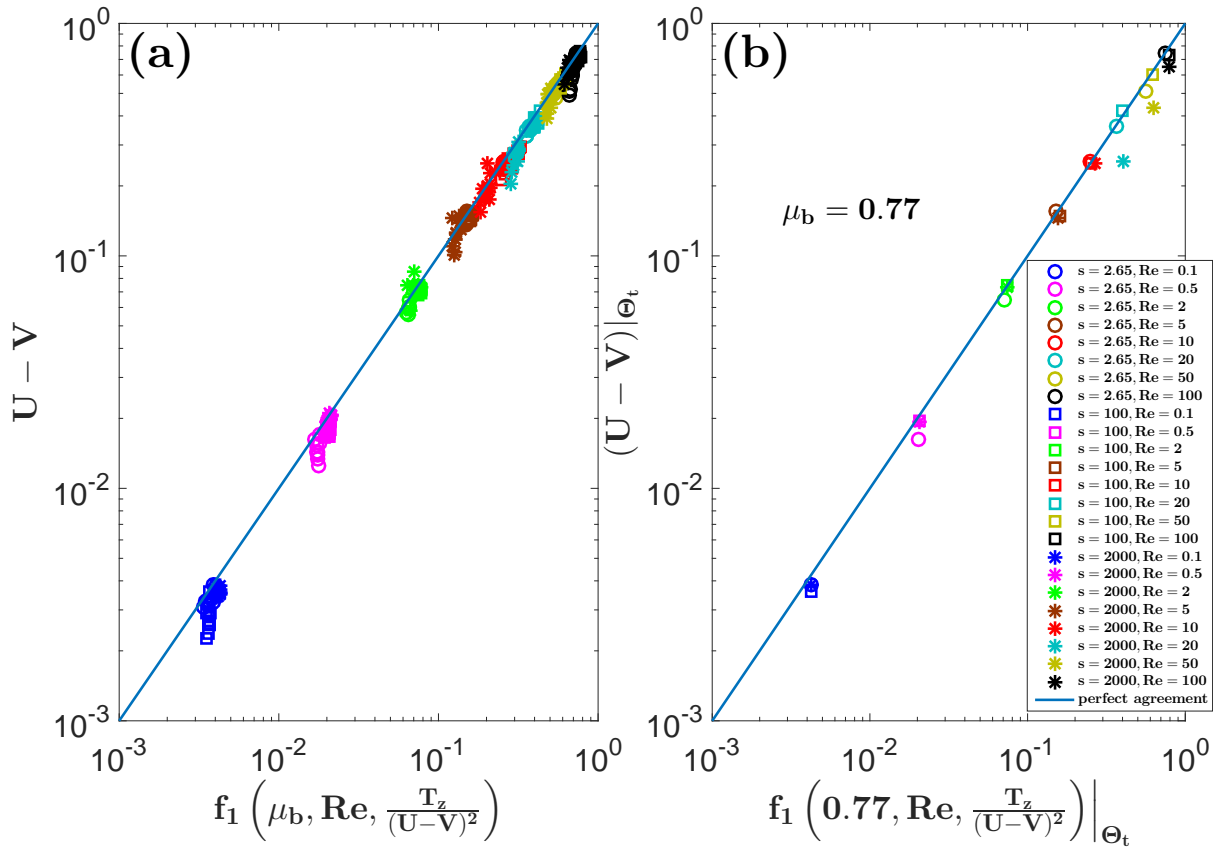


Figure S2: (a)  $U - V$  versus  $f_1(\mu_b, \text{Re}, T_z/(U - V)^2)$  using simulated values of  $\mu_b$  for varying  $s$ ,  $\text{Re}$ , and  $\Theta$ . (b)  $U - V$  versus  $f_1(\mu_b, \text{Re}, T_z/(U - V)^2)$  using  $\mu_b = 0.77$  for varying  $s$  and  $\text{Re}$  under threshold conditions ( $\Theta = \Theta_t$ ).

## Evaluation of the correlations between $V$ , $U$ , and $T_z$

Fig. S3 shows that the ratio  $V/U$  remains approximately constant with  $\Theta/\Theta_t$ , and that it can be described by a function of  $\lambda|_{\Theta_t}^2 \sqrt{\Theta_t}$ , where  $\lambda = \overline{\langle a_x \rangle^q} / \overline{\langle a_x \rangle}$  is the correctional quantity mentioned in the paper, reading

$$V/U \approx \beta_1(1 - \exp(-\beta_2 \lambda|_{\Theta_t}^2 \sqrt{\Theta_t})). \quad (\text{S21})$$

It also shows the approximation  $\lambda = 1$ , for which Eq. (S21) becomes Eq. (2) of the paper. Although this approximation significantly weakens the agreement, the influence on the final prediction of  $\Theta_t$  is small.

Moreover, Fig. S4 shows that

$$T_z \approx \alpha \lambda^{-1} \mu_b^{-2} V^2 \quad (\text{S22})$$

is consistent with the simulation data under threshold conditions. It also shows the approximation  $\lambda = 1$ , for which Eq. (S22) becomes Eq. (3) of the paper.

## The law of the wall

We use the version of the “law of the wall” by Ref. (10), reading

$$\begin{aligned} \frac{u_x}{\sqrt{(s-1)gd}} &= \sqrt{\Theta_t} f_2(\text{Re}_b, z/d), \\ f_2(\text{Re}_b, z/d) &= 7 \arctan \frac{\text{Re}_b z/d}{7} + \frac{7}{3} \arctan^3 \frac{\text{Re}_b z/d}{7} - 0.52 \arctan^4 \frac{\text{Re}_b z/d}{7} \\ &+ \ln \left[ 1 + \left( \frac{\text{Re}_b z/d}{C} \right)^{(1/\kappa)} \right] - \frac{1}{\kappa} \ln \left\{ 1 + 0.3 \text{Re}_b \left[ 1 - \exp \left( -\frac{\text{Re}_b}{26} \right) \right] \right\}, \end{aligned} \quad (\text{S23})$$

where  $\kappa = 0.4$  and  $C = \exp(16.873\kappa - \ln 9)$ . We use this “law of the wall” because it provides a single equation valid in all regimes. Indeed, within the viscous sublayer of the turbulent boundary layer, it corresponds to  $\tilde{u}_x = \sqrt{\Theta_t} \text{Re}_b z/d$ ; within the log-layer, it corresponds to  $\tilde{u}_x = \kappa^{-1} \sqrt{\Theta_t} \ln(z/z_o)$  with the roughness  $z_o/d = \text{Re}_b^{-1}/9$  in the hydraulic smooth and  $z_o =$

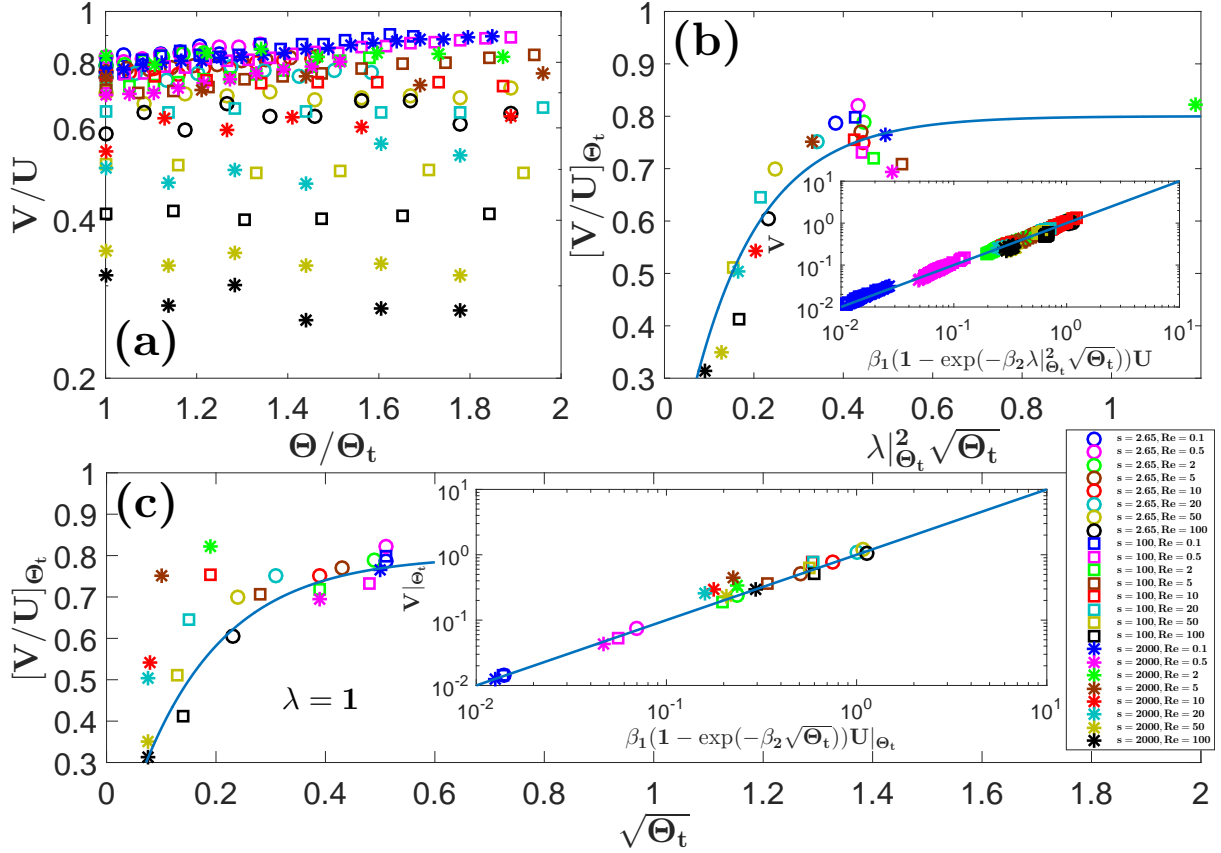


Figure S3: (a)  $V/U$  versus  $\Theta/\Theta_t$  for varying  $s$  and  $\text{Re}$ . (b & c)  $V/U$  versus  $\lambda|^2_{\Theta_t} \sqrt{\Theta_t}$  using (b) simulated values of  $\lambda|_{\Theta_t}$  and (c)  $\lambda|_{\Theta_t} = 1$  for varying  $s$  and  $\text{Re}$ . Insets: (b)  $V$  versus  $\beta_1(1 - \exp(-\beta_2 \lambda|^2_{\Theta_t} \sqrt{\Theta_t}))U$  using simulated values of  $\lambda|_{\Theta_t}$  for varying  $s$ ,  $\text{Re}$ , and  $\Theta$ . (c)  $V$  versus  $\beta_1(1 - \exp(-\beta_2 \lambda|^2_{\Theta_t} \sqrt{\Theta_t}))U$  using  $\lambda|_{\Theta_t} = 1$  for varying  $s$  and  $\text{Re}$  under threshold conditions ( $\Theta = \Theta_t$ ). The solid line corresponds to Eq. (S21).

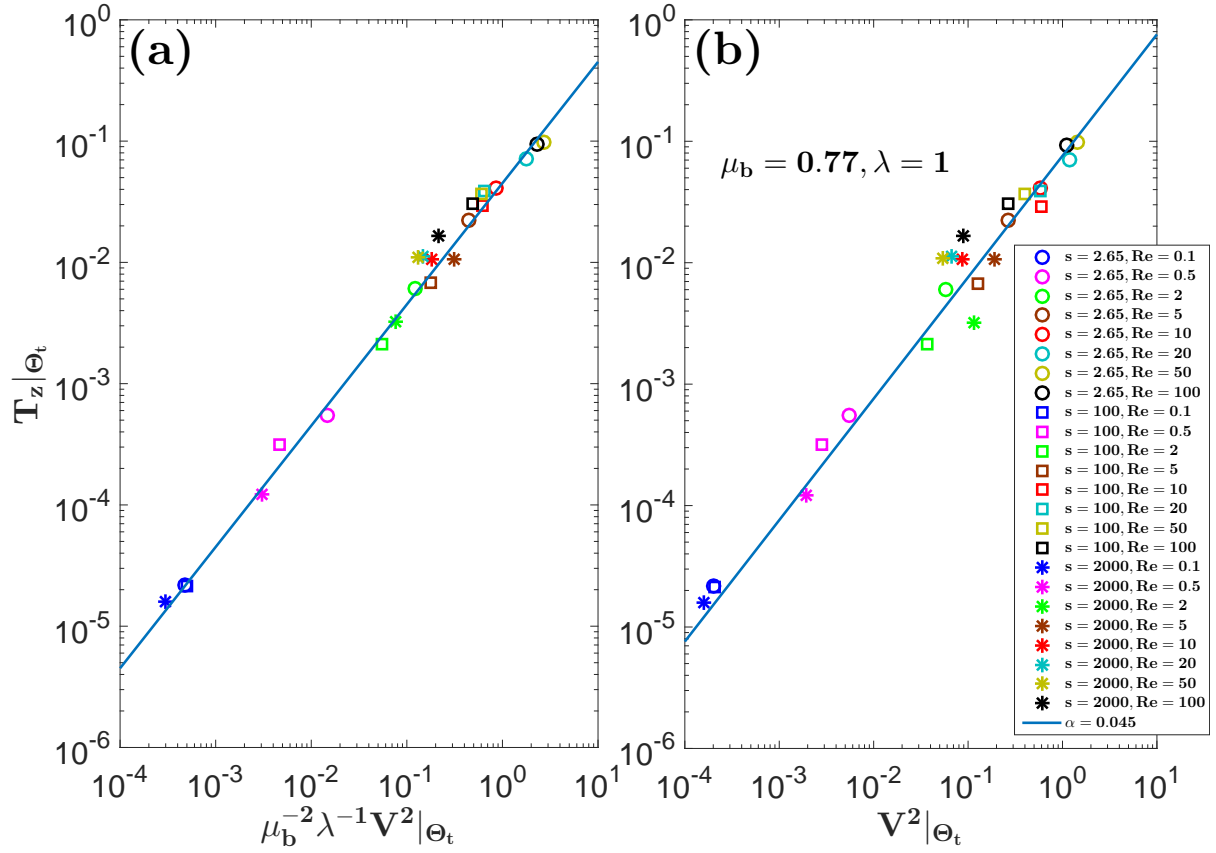


Figure S4: (a)  $T_z$  versus simulated  $\lambda^{-1} \mu_b^{-2} V^2$  for varying  $s$  and  $Re$  under threshold conditions ( $\Theta = \Theta_t$ ). (b)  $T_z$  versus simulated  $V^2$  for varying  $s$  and  $Re$  under threshold conditions ( $\Theta = \Theta_t$ ). The solid line corresponds to Eq. (a1) with (a)  $\alpha = 0.045$  and with (b)  $\alpha = 0.045$ ,  $\mu_b = 0.77$ , and  $\lambda = 1$ .

$d/30$  in the hydraulic rough regime (10). It is also valid within the transition between these regimes (10).

### The mean fluid velocity ( $U$ )

Eq. (4) of the paper involves the approximation  $\overline{\tilde{u}_x(z/d)} \approx \tilde{u}_x(Z)$ . This approximation is exact if  $\tilde{u}_x$  is linear in  $z/d$ . We find that the introduced error in non-linear regimes can be well compensated through the factor  $\lambda$  by

$$U = \lambda^{-1} \tilde{u}_x(\lambda Z). \quad (\text{S24})$$

Fig. S24 shows that Eq. (S24) is consistent with our simulations, including the entire range of simulated  $\Theta$ . It also shows the approximation  $\tilde{u}_x(z/d) = \sqrt{\Theta_t} f_2(\text{Re}\sqrt{\Theta_t}, z/d)$  under threshold conditions ( $\Theta = \Theta_t$ ) and  $\lambda = 1$ , for which Eq. (S24) becomes Eq. (4) of the paper.

### Derving an expression for $Z$

Using partial integration, Eqs. (S5) and (S11), and  $a_z \approx -\tilde{g}/(1+c_m/s)$ , we derive an expression for  $Z$  via

$$\begin{aligned} \int_{z_s}^{\infty} \rho \langle a_z \rangle z dz &= -P_{zz}(z_s) z_s - \int_{z_s}^{\infty} P_{zz} dz, \\ -P_{zz}(z_s) &= \int_{z_s}^{\infty} \rho \langle a_z \rangle dz \\ \Rightarrow \overline{\langle a_z \rangle (z - z_s)} &= -\overline{P_{zz}/\rho} \\ \Rightarrow Z &\approx \frac{z_s}{d} + (1 + c_m/s) \frac{\overline{P_{zz}/\rho}}{\tilde{g}d}. \end{aligned} \quad (\text{S25})$$

Then, through defining  $Z_c = z_s/d + (1 + c_m/s) \overline{P_{zz}^c/\rho}/(\tilde{g}d)$  and using Eqs. (S6-S8), Eq. (S25) becomes

$$Z = Z_c + (s + c_m) T_z, \quad (\text{S26})$$

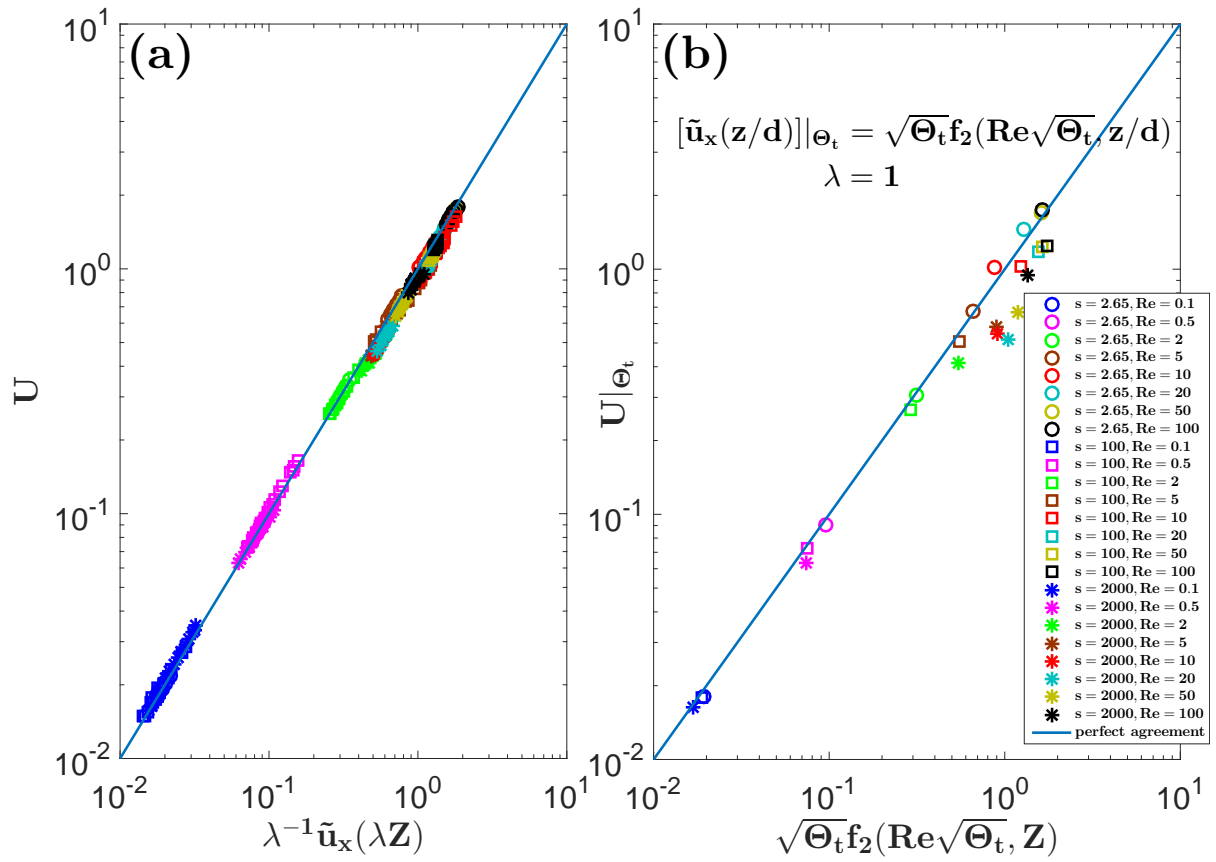


Figure S5:  $U$  versus (a)  $\lambda^{-1}\tilde{u}_x(\lambda Z)$  and (b)  $\sqrt{\Theta_t}f_2(\text{Re}\sqrt{\Theta_t}, Z)$  for varying  $s$  and  $\text{Re}$ . (a) shows the entire range of simulated  $\Theta$ , while (b) shows threshold conditions ( $\Theta = \Theta_t$ ).

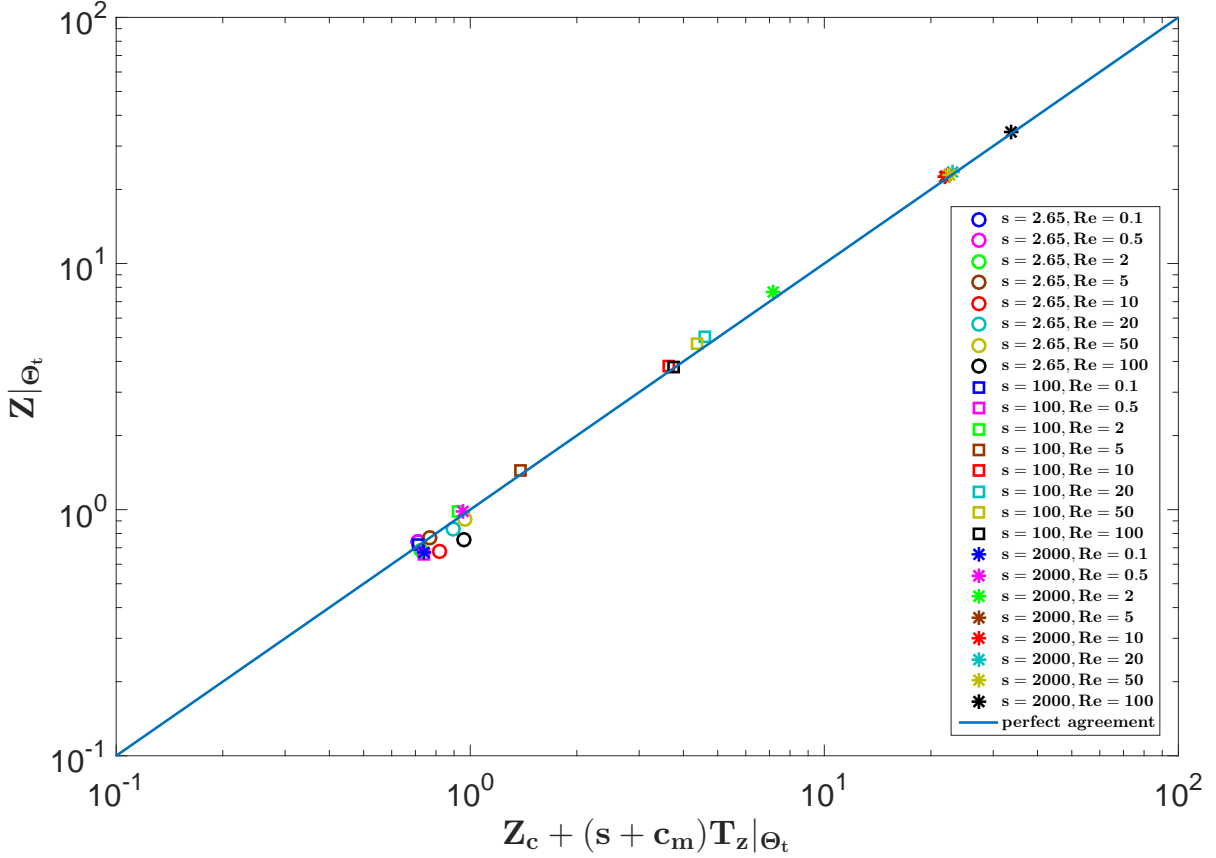


Figure S6:  $Z$  versus  $Z_c + (s + c_m)T_z$  using  $c_m = 0$  (numerical model neglects the added-mass force) for varying  $s$  and  $Re$  under threshold conditions ( $\Theta = \Theta_t$ ).

which is the same as Eq. (5) of the paper if the added-mass force is considered ( $c_m = 0.5$ ). Fig. S6 shows that Eq. (S26) using the constant value  $Z_c = 0.71$  is consistent with the simulation data under threshold conditions ( $\Theta = \Theta_t$ ).

### A complexer model including the calculation of $\lambda$

The analytical model presented in the paper consists of Eqs. (S21), (S22), and (S24) using  $\lambda = 1$ . Here we present an additional equation that allows the calculation of  $\lambda$ . It reads

$$U = \sqrt{\lambda}^{-3} \tilde{u}_x [\sqrt{\lambda} (Z_c + \gamma \sqrt{\lambda} (s + c_m) T_z)], \quad (S27)$$

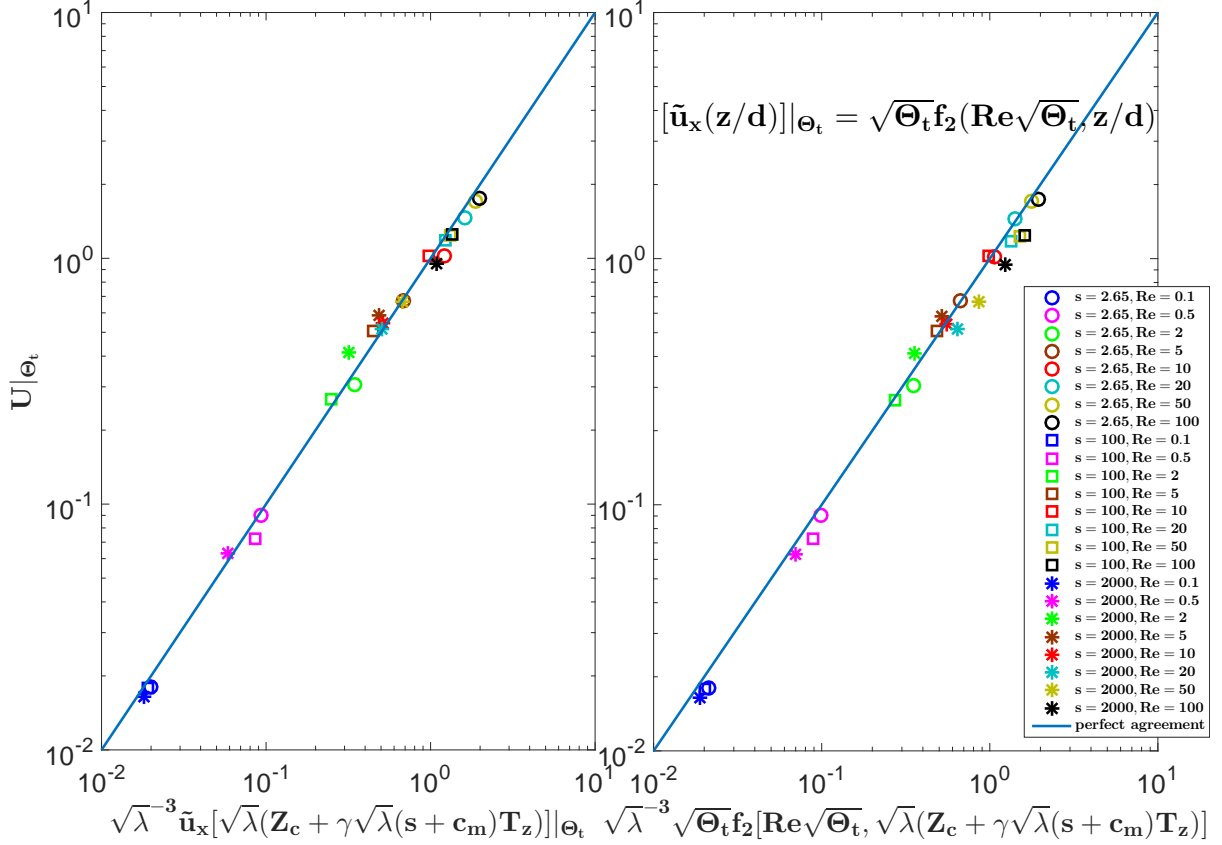


Figure S7:  $U$  versus (a)  $\sqrt{\lambda}^{-3} \tilde{u}_x[\sqrt{\lambda}(Z_c + \gamma\sqrt{\lambda}(s + c_m)T_z)]|_{\Theta_t}$  and (b)  $\sqrt{\lambda}^{-3} \sqrt{\Theta_t} f_2[\text{Re}\sqrt{\Theta_t}, \sqrt{\lambda}(Z_c + \gamma\sqrt{\lambda}(s + c_m)T_z)]$  for varying  $s$  and  $\text{Re}$ . (a) shows the entire range of simulated  $\Theta$ , while (b) shows threshold conditions ( $\Theta = \Theta_t$ ).

where  $\gamma = 1.3$  is an additional model parameter. Eq. (S27) is motivated through  $\lambda U = U_q$  (where  $U_q = \tilde{u}_x/\sqrt{(s-1)gd}$ ) and  $U_q = \sqrt{\lambda}^{-1} \tilde{u}_x(\sqrt{\lambda} Z^q)$  (where  $Z_q = \bar{z}^q/s$ ), which is analogous to Eq. (S24), but with a correction factor  $\sqrt{\lambda}$  rather than  $\lambda$ . Furthermore, we find  $Z_q = Z_c + \gamma\sqrt{\lambda}(s + c_m)T_z$ , which combined with the previous two relations gives Eq. (S27). Fig. S7 shows that Eq. (S27) is consistent with the simulation data for the entire simulated range of  $\Theta$ . It also shows the approximation  $\tilde{u}_x(z/d) = \sqrt{\Theta_t} f_2(\text{Re}\sqrt{\Theta_t}, z/d)$  under threshold conditions ( $\Theta = \Theta_t$ ), which is also used in the complexer model. Here is a summary of the model

equations of the complexer model:

$$U - V = f_1(\mu_b, \text{Re}, T_z/(U - V)^2), \quad (\text{S28})$$

$$V/U = \beta_1(1 - \exp(-\beta_2\lambda^2\sqrt{\Theta_t})), \quad (\text{S29})$$

$$T_z = \alpha\lambda^{-1}\mu_b^{-2}V^2, \quad (\text{S30})$$

$$U = \lambda^{-1}\sqrt{\Theta_t}f_2(\text{Re}\sqrt{\Theta_t}, \lambda Z), \quad (\text{S31})$$

$$Z = Z_c + (s + 0.5)T_z, \quad (\text{S32})$$

$$U = \sqrt{\lambda}^{-3}\sqrt{\Theta_t}f_2[\text{Re}\sqrt{\Theta_t}, \sqrt{\lambda}(Z_c + \gamma\sqrt{\lambda}(s + c_m)T_z)]. \quad (\text{S33})$$

Note that it follows from Eqs. (S31) and (S33) that  $\lambda \leq \gamma^2$ . In particular, the original and complexer model become identical when  $\gamma \rightarrow 1^+$ .

### Predicted versus simulated thresholds

Fig. S8 shows that the predictions of  $\Theta_t$  from both the original and the complexer model are consistent with simulation data, but the complexer model performs significantly better.

### Planetary predictions from the complexer model

Figs. S9 and S10 show the same predictions as Figs. 3 and 4 of the paper, but calculated from the complexer model.

### Asymptotic predictions

It is possible to strongly simplify both analytical models for certain cases. For instance, for sufficiently small  $\text{Re}$  and  $\Theta_t$ ,  $U - V \approx \mu_b\text{Re}/18$ ,  $U \approx \Theta_t\text{Re}Z$ , and  $V/U \approx \beta_1\beta_2\lambda^2\sqrt{\Theta_t}$ . The latter can be further approximated to  $U \approx U - V$  and  $V \approx \beta_1\beta_2\lambda^2\sqrt{\Theta_t}(U - V)$  in these cases. Moreover, cases with small  $\Theta_t$  usually correspond to large transport layers, for which

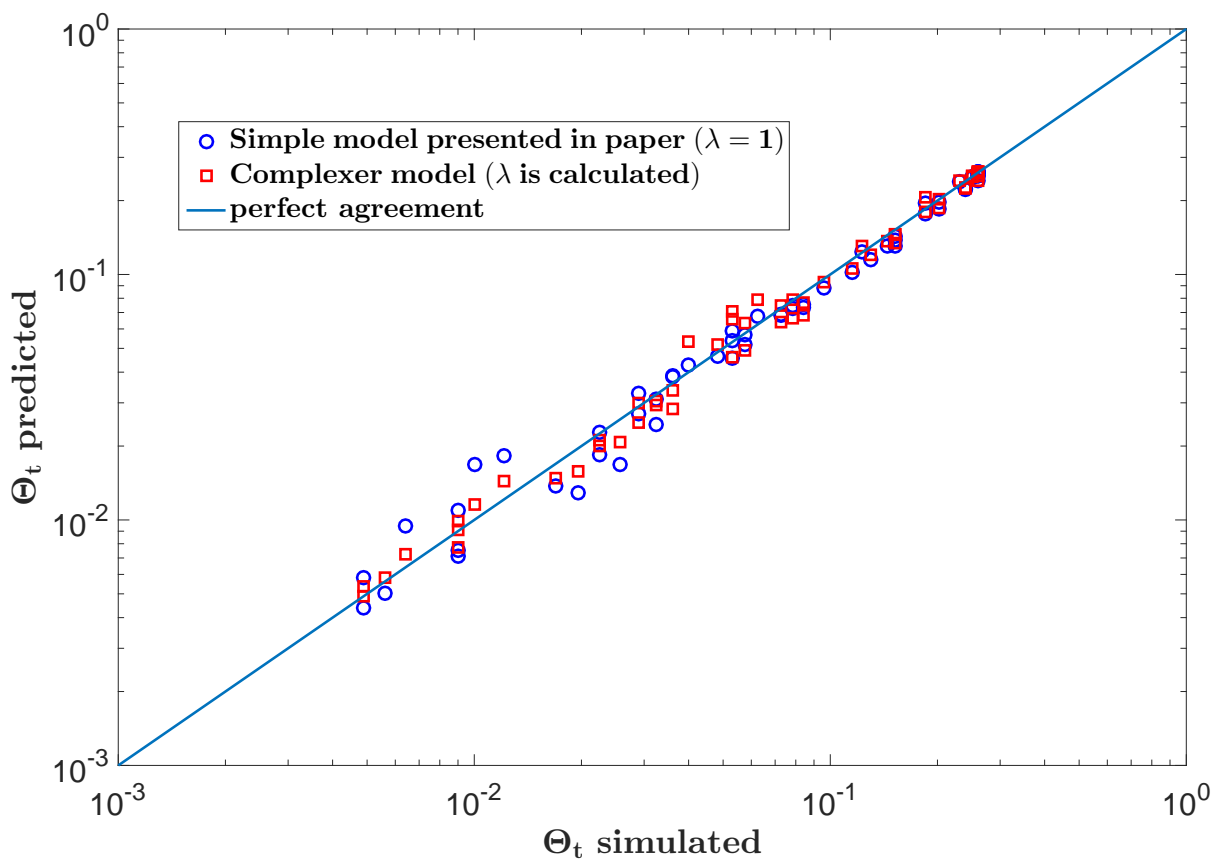


Figure S8: Predicted  $\Theta_t$  from the original model (blue circles) and the complexer model (red squares) versus simulated  $\Theta_t$ .

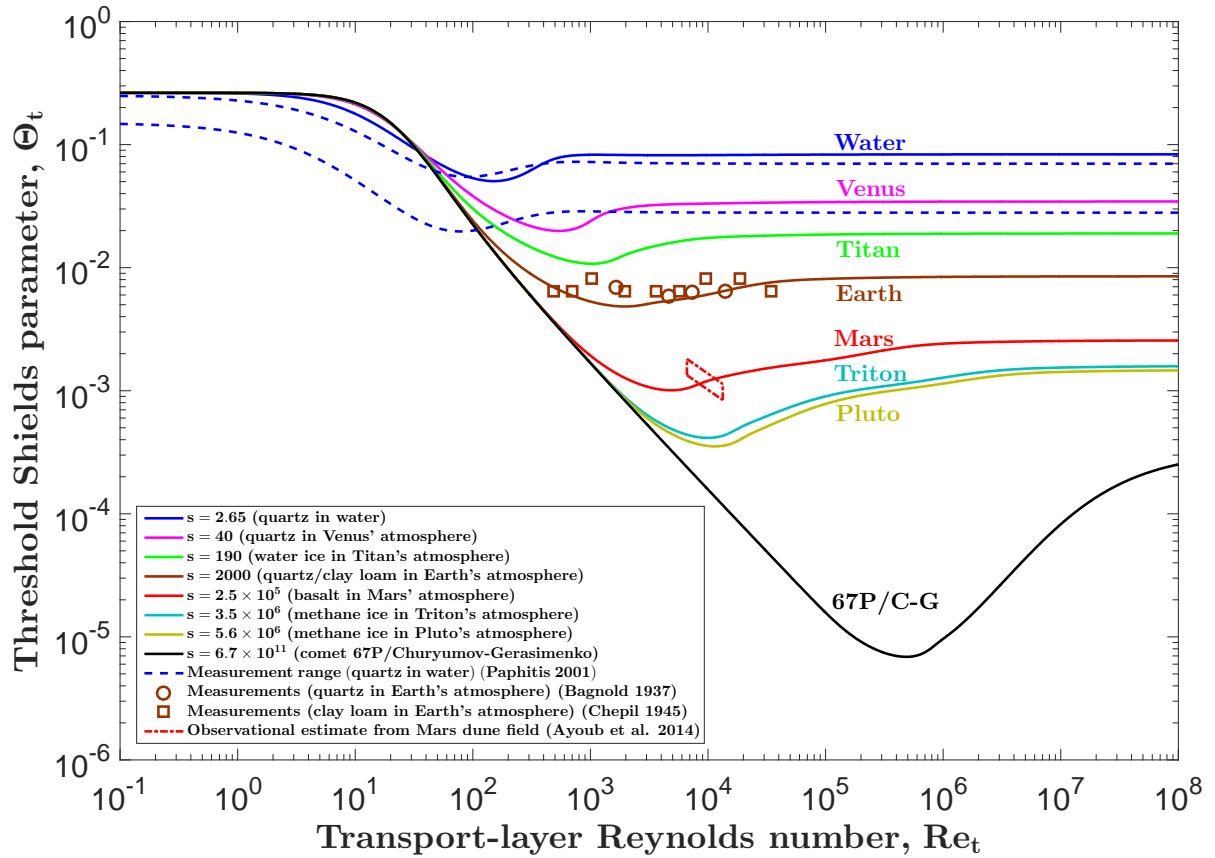


Figure S9: The threshold Shields parameter ( $\Theta_t$ ) in various environments predicted by the complexer model (solid lines), measured in water (13) (dashed lines) and Earth's atmosphere (15, 16) (symbols) for cohesionless sediments, and observationally estimated from seasonal variations of  $Q$  on Mars (28) versus the transport-layer Reynolds number ( $Re_t$ ).

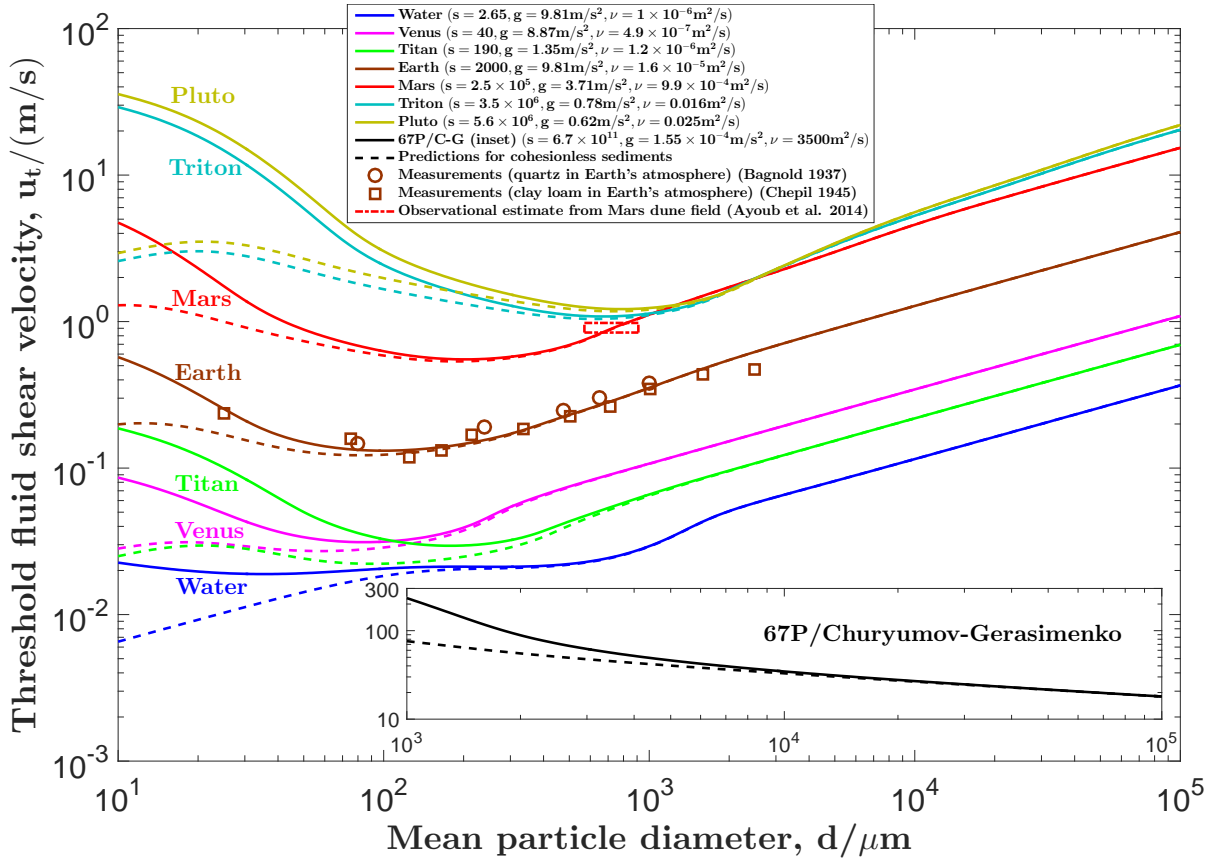


Figure S10: The threshold fluid shear velocity ( $u_t$ ) in various environments predicted by the complexer model corrected (solid lines) and uncorrected (dashed lines) for cohesive interparticle forces versus the mean particle diameter ( $d$ ). The symbols correspond to measurements in Earth's atmosphere (15, 16) and the red, dash-dotted lines to an observational estimate from seasonal variations of  $Q$  on Mars (28).

$Z \approx sT_z = \alpha\mu_b^{-2}\lambda^{-1}sV^2$ . Using  $\text{Re}_t = \text{Re}\sqrt{s}$ , these relations combined give

$$\Theta_t \approx \sqrt{\frac{18\mu_b}{\alpha\beta_1^2\beta_2^2\lambda^3}} \text{Re}_t^{-1}, \quad (\text{S34})$$

which corresponds to the dotted line in Fig. 3 of the paper (where  $\lambda = 1$ ). Eq. (S34) cannot be obeyed indefinitely with increasing  $\text{Re}_t$ . At some critical value of  $\text{Re}_t$ ,  $Z$  will exceed the viscous sublayer and enter the buffer layer. This is when  $U \approx \Theta_t \text{Re}Z$  is more and more violated, resulting in a minimum in  $\Theta_t$ . The point at which this happens is characterized by a critical viscous height

$$\frac{C_\nu}{\text{Re}\sqrt{\Theta_t}} = \frac{C_\nu\sqrt{s}}{\text{Re}_t\sqrt{\Theta_t}} = Z \approx \left(\frac{\alpha\beta_1^2\beta_2^2\lambda^3}{324}\right) \text{Re}_t^2 \Theta_t, \quad (\text{S35})$$

where  $C_\nu$  is a number between about 5 and 30, corresponding to the buffer layer. Combining Eqs. (S34) and (S35) gives

$$\min_{\text{Re}_t} \Theta_t(\text{Re}_t, s) \approx \left(\frac{\mu_b^3}{18C_\nu^2\alpha\beta_1^2\beta_2^2\lambda^3}\right)^{1/3} s^{-1/3}, \quad (\text{S36})$$

which corresponds to the curve shown in the inset of Fig. 3 of the paper (where  $\lambda = 1$ ) when  $C_\nu = 9$ .

## Movies

### Movie S1

Time evolution of the simulated particle-fluid system for  $s = 1.2$ ,  $\text{Re} = 5$ , and  $\sqrt{\Theta} = 0.44 \approx \sqrt{\Theta_t}$ . The flow velocity is shown as a background color with warm colors corresponding to high velocities and cold colors to small velocities. The horizontal and vertical axes are measured in mean particle diameters. Only 1/4 of the simulated horizontal domain is shown. That is why particles occasionally enter the system from the left. This is an example for sediment transport sustained predominantly through fluid entrainment.

## Movie S2

Time evolution of the simulated particle-fluid system for  $s = 100$ ,  $Re = 50$ , and  $\sqrt{\Theta} = 0.13 \approx \sqrt{\Theta_t}$ . The flow velocity is shown as a background color with warm colors corresponding to high velocities and cold colors to small velocities. The horizontal and vertical axes are measured in mean particle diameters. Only 1/4 of the simulated horizontal domain is shown. That is why particles occasionally enter the system from the left. This is an example for sediment transport sustained predominantly through particle-bed-impact entrainment.

## Movie S3

Time evolution of the simulated particle-fluid system for  $s = 2000$ ,  $Re = 2$ , and  $\sqrt{\Theta} = 0.18 \approx \sqrt{\Theta_t}$ . The flow velocity is shown as a background color with warm colors corresponding to high velocities and cold colors to small velocities. The horizontal and vertical axes are measured in mean particle diameters. Only 1/4 of the simulated horizontal domain is shown. That is why particles occasionally enter the system from the left. This is an example for sediment transport sustained predominantly through particle-bed-impact entrainment.